technische universität
dortmund

Advanced Laboratory Course

Particle Physics

Measurement of scintillating fibres for the LHCb experiment

Koen Denekamp & Riana Shaba

Advisor: Jonas Rönsch

May 2025

Contents

1 Introduction

1.1 The LHCb detector

Here we will give a brief overview of the LHCb detector at CERN.
The LHCb detector was conceived specifically to perform experiments in flavour physics. According to the 2003 design specifications [8], it was created to study CP-violation and other phenomena related to the b quark, hence the name LHCb.
The LHCb detector, shown in Fig. 1, has several components. In this diagram, the protons collide at the left, where $z = 0$, and in the middle, where $y = 0$. The particles created in the collision will thus be detected if they move from left to right. It should be noted that particles are created in every direction, but particles containing b and c quarks mostly move in the z or negative z direction. This is the order that will be followed in explaining the different components as well. The $z-$coordinate is important later in the project, as one of the variables depends on this.

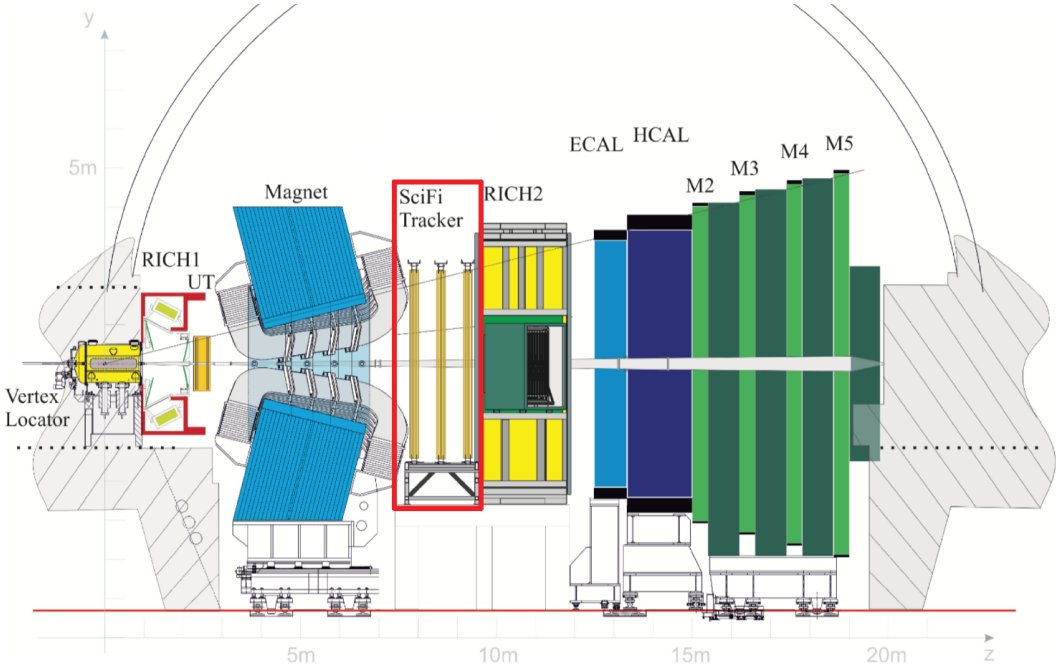

Figure 1: Diagram of the LHCb detector with the separate components. From Ref. [9].

The decaying particles first encounter the Vertex Locator, often abbreviated as VELO.

This segment is part of the tracking system, as it both reconstructs primary and secondary vertices of particles, their decays, and the trajectories (tracks) [6].
Then the particles enter RICH1. This is an abbreviation for Ring-Imaging Cherenkov (detector) 1. This part of the detector is used for particle identification [1]. Based on the Cherenkov angle between the track of the particle and the line one can draw across the side of the rings, the velocity of the particle can be determined [2].
Since the momentum of the particle is measured using the tracking stations, and the magnet for charged particles [2], it is possible to combine the momentum and velocity measures to find an estimate of the mass of a particle.
Then there is a magnet. This magnet is used to measure whether a particle is positively, negatively, or neutrally charged, as these groups of particles will bend in different directions, or not at all for neutrally charged particles. It is also used to calculate the momentum of charged particles since high-momentum particles bend less than low-momentum particles.
Then, starting from Run 3, the particles encounter the Scintillating Fibre (SciFi) tracking detector system. This is the system considered in this report, and the inner workings will thus be explained in more detail in Sec. 2.
Then another RICH detector is encountered, before entering the SPD/PS layers. SPD stands for Scintillator Pad Detector, while PS stands for PreShower. The goal of the SPD is to identify charged particles and to separate electrons from protons. The PS identifies electromagnetic particles. These steps are taken, since the calorimeters that follow these layers require good background rejection and reasonable efficiency [10].
There are two calorimeters. One specifically for electrons and photons, known as the ECAL and one for hadrons, known as the HCAL. These detectors measure the energy of the incoming particles.
Lastly there are the five muon detector layers, which are also part of the tracking system. Muons fly through the other layers almost unhindered, but this is where they are finally measured.

2 Scintillating Fibre Tracker

2.1 Structure of Scintillating Fibres

The LHCb Scintillating Fibre Tracker (SciFi) consists of three stations, each with four detection planes arranged one behind the other. It is a high-resolution detector that covers an area of 340m^2 [5].
From Figure 2 we can see the configuration of the tracking station and its layers. The detector has around 10 to 12 individual modules, where each module consists of 8 fibre

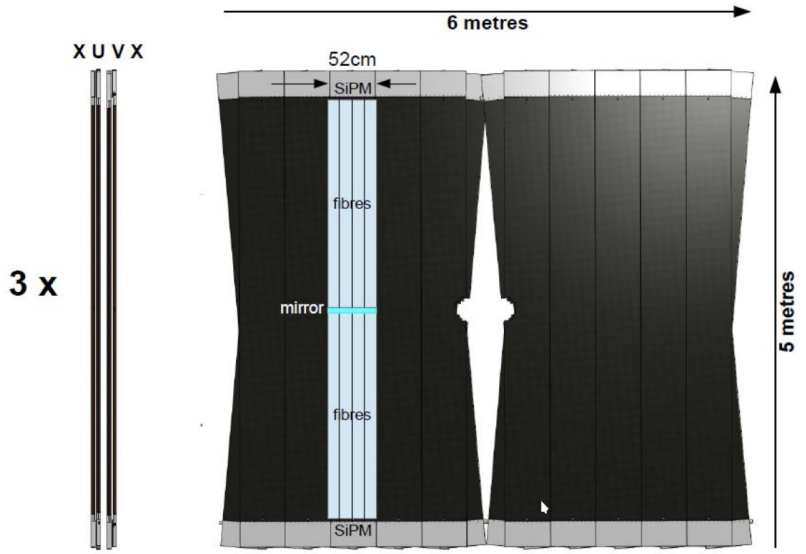

Figure 2: Schematic view of one SciFi Tracking station. The left shows a *yz*-view, and the right side a *xy*-view or front view. It consists of 4 layers, where each layer is made of 10 or 12 individual fibre modules, consisting of 8 fibre mats with a length of 2.5m. All 4 layers are positioned in a *x_u_v_x* pattern. From Ref. [5].

mats with a length of 2.5 m each. Fibre mats are simply the scintillating fibres arranged in a hexagonal structure, held together with epoxy glue. So in the fibre mats there are 6 fibre layers of very densely-packed scintillating fibres with a diameter of 250µm each. They have a 220µm thick polystyrene core, an organic scintillator that acts as the active detector medium, and around the core there are two sheaths, with outwardly decreasing refractive indicies to allow for total internal reflection, and a thickness of 7.5µm each. The four layers are placed in a *x_u_v_x* pattern. Fibres in the x orientation run vertically and are tilted by ± 5° in the u- and v- layers. Each layer has 40 mats side by side and two on top of each other. The scintillation light is detected by the readout electronics placed only on one end of the mat, and a mirror is glued on the other end to reflect photons to the SiPMs (Silicon Photomultipliers) to increase the light yield and maximize the signal amplitude.

2.2 Working Principle and Silicon Photomultipliers

The fibre made of polystyrene core, has an added dye p-terphenyl to increase the quantum yield and a wavelength shifter to increase the attenuation length.
As soon as an ionising particle passes through the fibre, the valence electrons of the polystyrene get excited. This means they are delocalised and can move freely throughout the molecule, such as moving to higher energy levels upon excitation. Then from the de-excitation, a photon is emitted with an energy that is the same as the difference between the energy levels.
However, the photons emitted from the scintillator have an attenuation length of around 1 m, which is not enough considering that the fibres are 2.5 m long. A minimum attenuation length of 3 m is enough to ensure that photons reach the readout electronics, and for this purpose the wavelength shifter is used for the absorption spectrum to correspond as closely as possible to the emission spectrum of p-terphenyl. It aborbs and emits photons at higher wavelengths, where the fibres have a greater attenuation length.
As mentioned previously, the silicon photomultipliers (SiPMs) are placed at the end of the fibre mats to measure the photons and convert the light into a measurable, digital signal. The fibres are read by 128-channel arrays with individual size of 0.25×1.62 mm [5] shown in Figure 3b, divided into 57.7×62.5 µm sized pixels, each representing a reverse biased pn junction. If a photon hits a pixel, it can generate an electron-hole pair which is then separated and accelerated due to the high electric field it feels because of the high voltage that is applied. The energy that these electrons gain during the acceleration can trigger more electrons and produce an avalanche effect of about 10^6 electrons. It can happen that several photons can hit the same pixel trigger, and therefore trigger the same signal as a single photon would do, hence the pixel size needs to be minimised properly. In Figure 2 there's a visual representation of the process that starts as soon as a charged particle traverses the fibre. It can be seen that not all photons are detected, and that there are some pixels with more than one hit, as well as photons hitting the free area between the channels.
The SiPM provides photon detection efficiency around 43% at maximum, and a relatively low noise. To suppress dark noise after irradiation that comes from the dark current rate, the SiPMs are cooled to -40°C during operations to mitigate damages. They are mounted in such a way that they measure all the light emerging from the end of the fibre at the same time, so the readout measures effective attenuation over all wavelengths. A spectrometer is used to investigate the dependence of the attenuation on the wavelength and the angle.
The SciFi tracker achieves a spatial resolution of less than 100 µm, and a hit efficiency of $\geq 99\%$ [3]. They are inexpensive and can cover a large area on the detector. With the several adavantages it offers, this detector element boosts selection efficiency for numerous

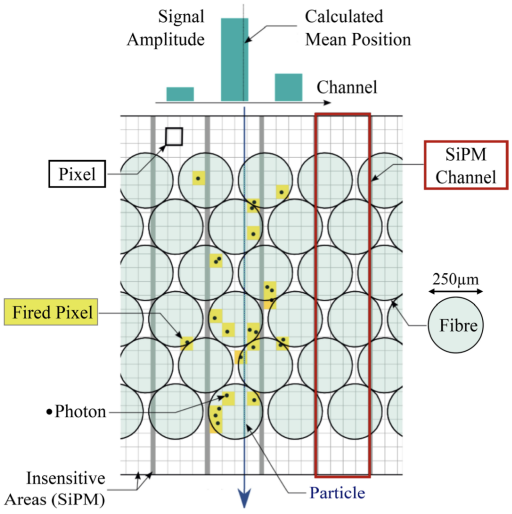

(a) Visual representation of a charged particle passing through a layer and generating a signal. Taken from Ref. [7].

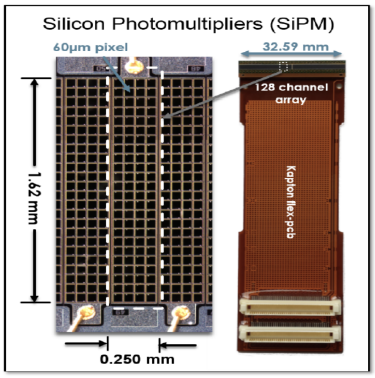

(b) Single SiPM channel and a 128-channel SiPM array. Taken from Ref. [5].

physics event types and provides a great improvement to the LHCb experiment.

3 Experimental Setup

The measurements are done using a computer-controlled measuring device. This device, the spectrometer and the xy table are controlled by a central program.
The spectrometer can reach saturation, which is the case at approximately 65.000 counts. The room lights provides a small excitation of the fibre, so a signal is still measured despite the LEDs being switched off.
But with a dark current measurements before each data collection, it is possible to filter out this constant background excitation by subtracting it. Even when no light enters the spectrometer, a constant dark current signal of approximately 600 counts is still measured, and it needs to be subtracted from the actual counts.
The LED box can move along the fibre with the xy table, and cause excitations of the fibre. The y axis is not used.
There is a specially-developed device that can move the spectrometer along a horizontal and vertical angle. However, this is not possible completely around the end of the fibre, as the device itself would collide with the fibre. Therefore, it can only scan the angular intervals [-20°, 90°] horizontally and [-6°, 90°] vertically.

4 Data Analysis

4.1 Spectrometer Measurement

In this section, we explore the light intensity of the photons produced from the excitation of the fiber by the room light. The measurements are carried out by a spectrometer and a graphical user interface.
For each measurement, dark current signal has been measured and subtracted from the actual counts in order to get the "cleaned" intensity. The first spectrometer measurement was performed at an angle of 0°, with the room light switched off. The intensity of the light is plotted against the wavelength as it can be seen in Figure 4. On the left side 4a we have shown all the counts without removing the background with respect to the wavelength, while on the right side 4b we have shown the actual intensity with the dark counts removed.

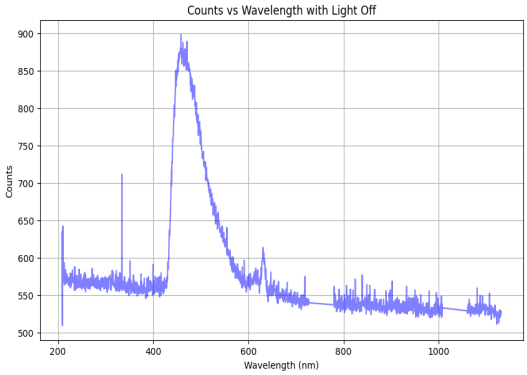

(a) This plot shows the counts against the wavelength for the room light switched off, without having removed the dark current counts.

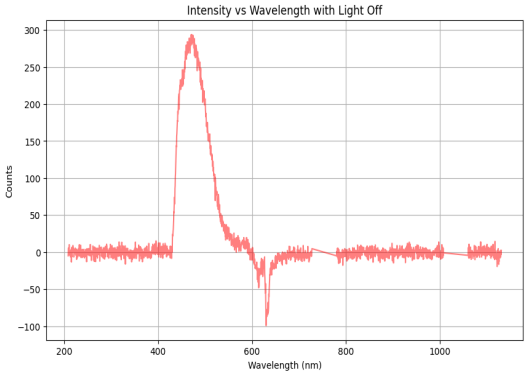

(b) This plot shows the intensity against the wavelength for the room light switched off, having removed the dark current counts.

Figure 4: Plots showing the light spectra before and after removing the dark counts.

The second spectrometer measurement was performed the same way, but this time with the room light switched on. The intensity of light against the wavelength for this case is shown in Figure 5. On the left side 5a we have shown all the counts without removing the background with respect to the wavelength, while on the right side 5b we have shown the actual intensity with the dark counts removed.
As expected both intensity spectra have the same shape, while in the case for the room

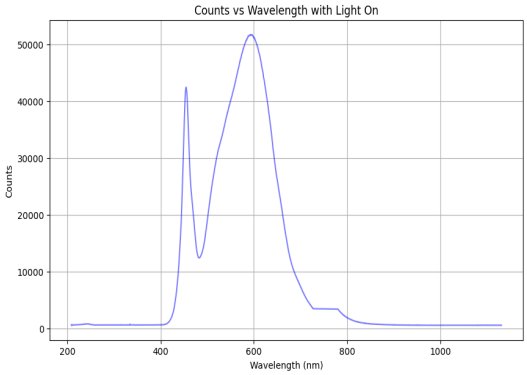

(a) This plot shows the counts against the wavelength for the room light switched on, without having removed the dark current counts.

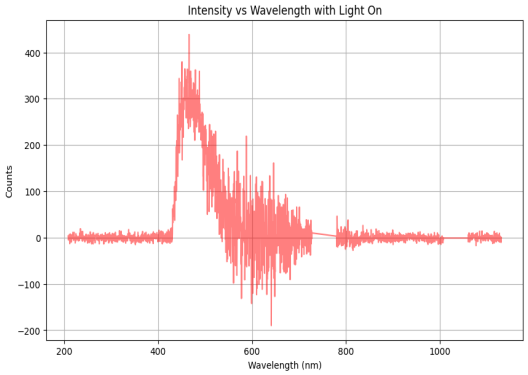

(b) This plot shows the intensity against the wavelength for the room light switched on, having removed the dark current counts.

Figure 5: Plots showing the light spectra before and after removing the dark counts.

being switched on, the first peak seen on the left side in Figure 5a is probably due to a laptop screen that was turned on when we took the measurement. The fluctuations that are still present in the intensity plot in Figure 5b, as the one before as well, are a result of the environmental photons that are present.

4.2 Radial Symmetry

In this section, we will confirm the radial symmetry of the fiber. To do this, we set a fixed excitation position of 0 mm, and a changing horizontal angle with a range of $(-18°, 30°)$, with 15 steps in between, and a range of $(-6°, 35°)$, also with 15 steps in between. Every combination of these steps were measured, so we have 225 different measurements. A 2D histogram of the distribution over the angles can be found in Fig. 6.

From the distribution here we can see that there is a radial symmetry, although the maximal intensity is not at $[0°, 0°]$ as ideally expected. This is probably because of the imperfect alignment of the spectrometer with respect to the fibre.

4.3 Simulation

The data considered in this section is simulated data, given in a `pickle` file. It contains 11,795,248 events of simulated photons interacting with the system. For each of these events, 15 variables are generated. We will introduce them as they become relevant.

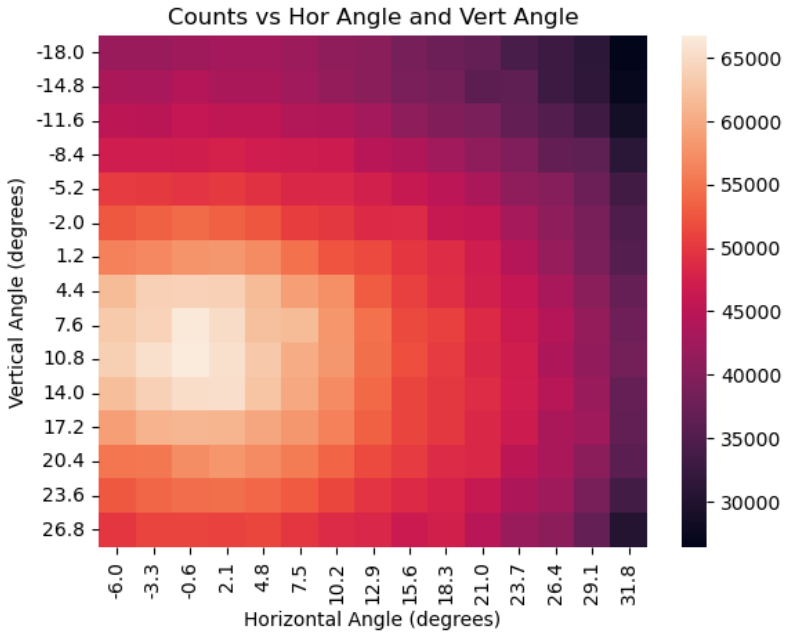

Figure 6: 2D histogram of the measured intensity over the vertical and horizontal angles.

The first step was to remove any nonphysical events, and for this there are two criteria. Firstly, we removed any photons that had an exit point further away from the center than the radius of the fiber. And secondly, we removed any photons that had caused Rayleigh scattering.

We then wanted to investigate the angle θ, which is the angle the photon makes with the x-axis, which is defined to be the center of the fiber. Since the momentum vector defined is normalized, this is simply the inverse cosine of the photon momentum in the x-direction, or

$$\theta = \arccos(p_{x,start}). \tag{1}$$

Additionally, we split the simulated data in two sets. One is a data set that only contains photons that stayed in the core of the fiber, and one is a data set that only contains photons that crossed into the cladding.

We can determine mathematically the maximum angle at which total internal reflection (TIR) can occur for meridional photons at the core-cladding interface, and the first cladding - second cladding interface.
First, we consider TIR on the core - cladding interface. A sketch of this case is shown on

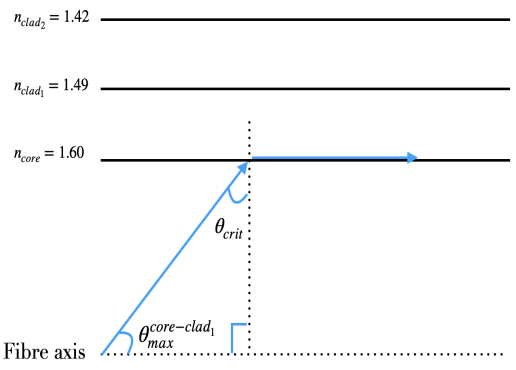

(a) Construction of the maximum polar angle at the core-cladding interface, $\theta_{\max}^{\text{core}-\text{clad}_1}$, for meridional photons during TIR.

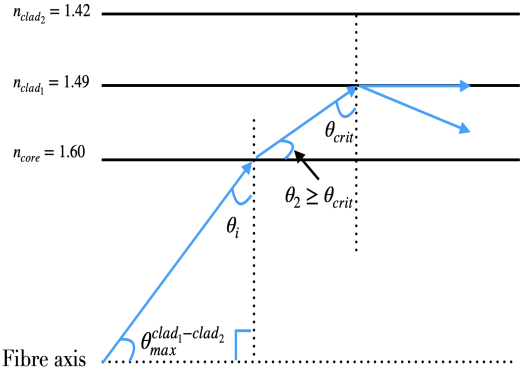

(b) Construction of the maximum polar angle at the first cladding-second cladding interface, $\theta_{\max}^{\text{clad}_1-\text{clad}_2}$, for meridional photons during TIR.

Figure 7: Sketches of the maximum polar angle for meridional photons during Total Internal Reflection (TIR). Two cases are considered, the first being when the TIR happens at the core - cladding interface, and the other when the TIR happens at the first cladding - second cladding interface.

Figure 7a.

For TIR to occur, the incident angle needs to be larger or equal to the critical angle, so we need to take the case where the incident angle is exactly as the critical one. Using Snell's Law and the fact that now the refracted ray of light is exactly at 90°, we get the following expression:

$$n_{core} \sin \theta_{crit} = n_{clad_1} \tag{2}$$

where n_{core} = 1.60 is the refractive index of the polystyrene core, n_{clad_1} = 1.49 is the refractive index of the first cladding layer and θ_{crit} is the critical angle.
From geometrical considerations, we can see that the maximum angle relative to the fibre axis that meridional photons need to have in order to be guided to the end of fibre by TIR in the core-cladding interface is:

$$\theta_{max}^{core-clad_1} = 90° - \arcsin\left(\frac{n_{clad_1}}{n_{core}}\right) = 21.4°. \tag{3}$$

In the second case, we consider the TIR to occur in the interface between the first cladding layer and the second cladding layer. We use the same reasoning as in the first case, where this time the incident angle from the first cladding needs to be exactly as the critical angle.

Again, we use Snell's Law to get the critical angle:

$$n_{clad_1} \sin\theta_{crit} = n_{clad_2}, \tag{4}$$

where n_{clad_2} = 1.42 is the refractive index of the second cladding layer.
Then we have to look at the core - first cladding interface to find the relation between the incident angle to this interface with the critical angle. From the incident angle, we can then calculate the maximum angle we are looking for. So again, we use Snell's law for this interface:

$$n_{core} \sin\theta_i = n_{clad_1} \sin\theta_{crit} \quad \rightarrow \quad \theta_i = \arcsin\left(\frac{n_{clad_2}}{n_{core}}\right), \tag{5}$$

where θ_i is the incident angle.
Using the relation for the critical angle in Equation 4, and from geometrical consideration, we find that the maximum angle relative to the fibre axis that meridional photons need to have in order to be guided to the end of fibre by TIR in the core-cladding interface is:

$$\theta_{max}^{clad_1-clad_2} = 90° - \theta_i = 27.4°. \tag{6}$$

In Fig. 8, we show the distribution of θ for the core and cladding photons, as well as the maximum angles.

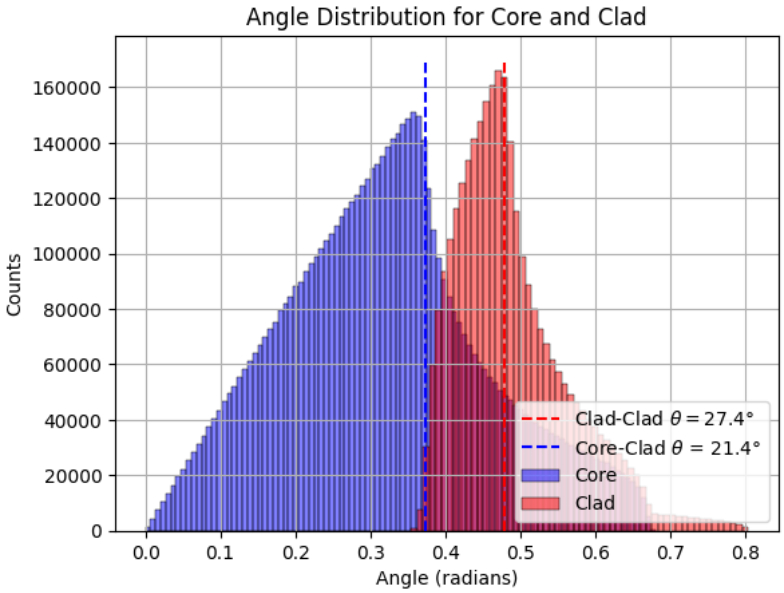

Figure 8: Plot showing two histograms of distributions of the angle θ for the core and cladding photons. The theoretical maximum angles for TIR to occur between the core-clad interface and first cladding-second cladding interface are shown as a threshold.

In both distributions we notice that they have similar shapes. Firstly, on the left side of the respective maximum angle, we notice a linear increase. This can be explained due to the fact that as the incident angle θ increases, a larger θ corresponds to a larger area of the scintillating fibre that is exposed to incoming photons. Secondly, on the right side of the respective angles, we see an exponential decrease. This happens because as the incident angle keeps increasing and getting larger than the critical angle, there will come a point when TIR will not occur anymore, and the photons will be lost, so the photon count experiences a noticeable drop. This behaviour aligns well with the theoretical maximum angle calculated for the TIR to occur in both interfaces considered, marking a threshold for both regions of the distributions.

Next, we define the minimum distance of the photons to the fibre centre from the distance of two lines. A sketch of this is shown in the Figure 9.

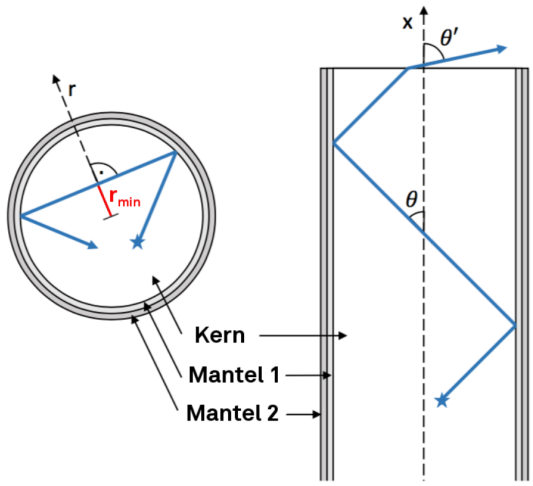

Figure 9: Geometry of non-meridional photons' trajectory through the fibre. A cross section image is shown on the left, and on the right a side view of the same trajectory is shown. From Ref. [4]

We define the position vector as follows:

$$\vec{p}(t) = \begin{pmatrix} x\_start \\ y\_start \\ z\_start \end{pmatrix} + t \begin{pmatrix} px\_start \\ py\_start \\ pz\_start \end{pmatrix} \qquad \vec{x}(s) = \begin{pmatrix} 0 \\ 0 \\ 0 \end{pmatrix} + s \begin{pmatrix} 1 \\ 0 \\ 0 \end{pmatrix} \tag{7}$$

where `x_start, y_start, z_start` are the coordinates where the photon was

created, and `px_start, py_start, pz_start` are the components of the momentum direction along the individual axes at the creation of the photon. The momentum is normalised.
We minimise the distance between the two lines defined above, and solving for t we find:

$$t = -\frac{y\_start \cdot py\_start + z\_start \cdot pz\_start}{py\_start^2 + pz\_start^2} \tag{8}$$

And it follows that the minimum distance then is:

$$r_{min} = \sqrt{t^2 \cdot (py\_start^2 + pz\_start^2)} \tag{9}$$

These calculations are performed for both core and cladding photons, and 2D histograms are created for each.

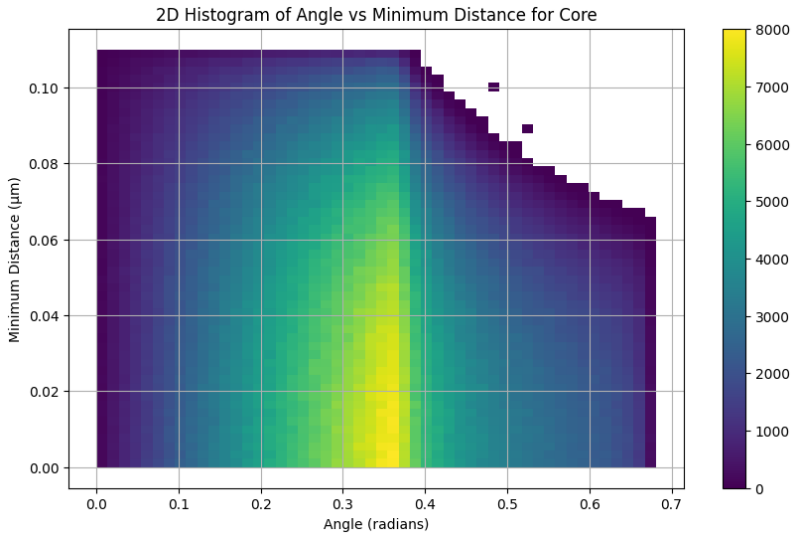

Figure 10: Plot showing a 2D histogram of the distribution of the minimum distance of core photons with respect to the angle of the photons relative to the fibre central axis.

In Figure 10 we have a 2D histogram of the distribution of the core photons with respect to the minimum distance. The heatmap indicates the counts of the photons for this case. It is noticeable that the region where the maximum angle is, $\theta \approx 0.37$rad, for the core-cladding interface, is the brightest. This matches with the reasoning made previously about the distribution of the angle with counts. As the minimum distance

r_{min} keeps increasing, the photon trajectory becomes more helical, meaning the photon travels closer to the fibre wall and reflects more frequently. This behaviour causes the photon to interact at increasingly shallow angles with the core interface. The angle to the interface, θ_{ref} under which TIR happens, is given by Equation 10.

$$\theta_{ref} = \arcsin\left(\sqrt{1 - \frac{r_{min}^2}{r_{core}^2}}\sin\theta\right) \tag{10}$$

Higher $r_{\min}$ values allow photons to remain within the fibre even at larger angles θ, which exceed the critical angle. However, we see that beyond a certain point there is a significant drop in the photon counts. This happens because when r_{min} goes close to the value of the radius of the core material, r_{core}, the photon is almost travelling parallel to the fibre wall. But the photons still needs to propagate and leave the fibre at some point. The angle θ cannot become too large because otherwise the longitudinal component along the fibre axis becomes too small, and the photon won't reach the end of the fibre. Therefore, physical constrains set limits on the fact that even if the minimum distance keeps increasing so much, the angle θ cannot become arbitrarily large, ensuring this way that the photons are guided through the fibre and manage to exit.

The same distribution is shown for the cladding photons as in Figure 11.

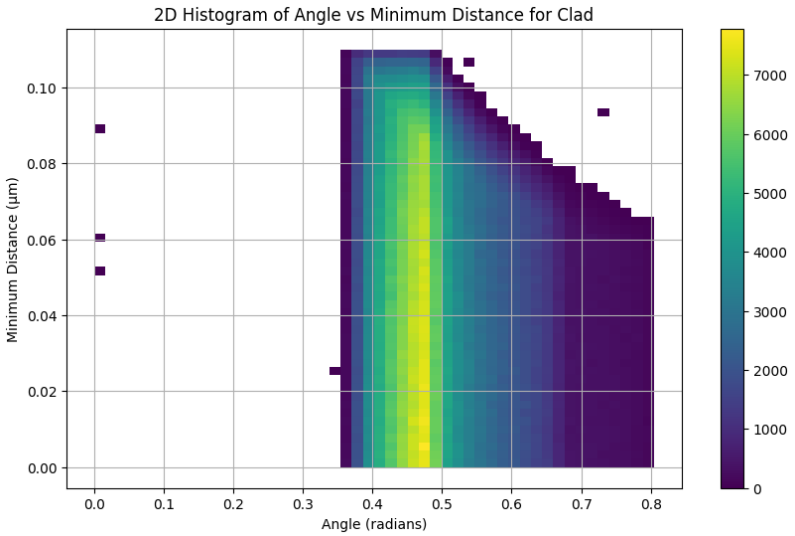

Figure 11: Plot showing a 2D histogram of the distribution of the minimum distance of cladding photons with respect to the angle of the photons relative to the fibre central axis.

Here the optical and geometric reasoning is the same, but in the case for cladding photons we see that there are almost no photons for every r_{min}, and for angles lower than $\theta \sim 0.37$rad, which is the maximum angle for TIR to occur in the core-cladding interface. This aligns with the expected behaviour, because for photons to reach the interface between the claddings, the TIR in the core-cladding interface has failed to occur. This is why we don't see photons for lower angles in the cladding, they remain trapped in the core. Then the histogram shows the same pattern, with the heatmap indicating the brightest region that corresponds to the maximum angle, $\theta \approx 0.43$rad. This reflects the fact that only photons at very high angles can escape from the core and reach the cladding. As the angle increases, there are more helical movements, increasing the minimum distance from the fibre axis and reflecing more frequently. Beyond a certain angle, the number of photons sharply decreases due to physical limits on propagation length and their escape from the fibre.

In the end, we wanted to see if the attenuation length was dependent on θ angle. In order to do this, we divided the data in 10 bins of increasing θ. We then fitted, to each distribution, the exponential decay

$$I(x) = I_0 e^{-\frac{x}{L}}, \tag{11}$$

where I_0 is an initial value, x is the position and L is the to be determined attenuation length. The result of this can be found in Fig. 12.
From this figure we can see that the attenuation lengths are found to be approximately above 5000 mm.

4.4 Intensity Measurement

In order to determine the attenuation length of the fiber in the laboratory, we performed an intensity measurement over different distances to the end of the fiber. Here we also varied the vertical angle over the range $(5^\circ, 35^\circ)$, with 10 steps in between. The x-value was varied from $(0, 2000)$ mm, with 20 steps in between. A plot of the intensities and different x-positions can be found in Fig. 13. Here we notice that there is not a smooth exponential decrease. It seems that there may be a fault in the fiber at around 600 mm. Due to this, it was decided that we would create two fits for two different splits, and leave a third split without a fit as this split would only contain two datapoints. The equation to be fitted is Eq. 11. The result of these fits is shown in Fig. 14. From these fits we get two values for the attenuation length: 4261.7 mm and 3044.8 mm. Taking the average, we obtain an attenuation length of 3653.28 mm.

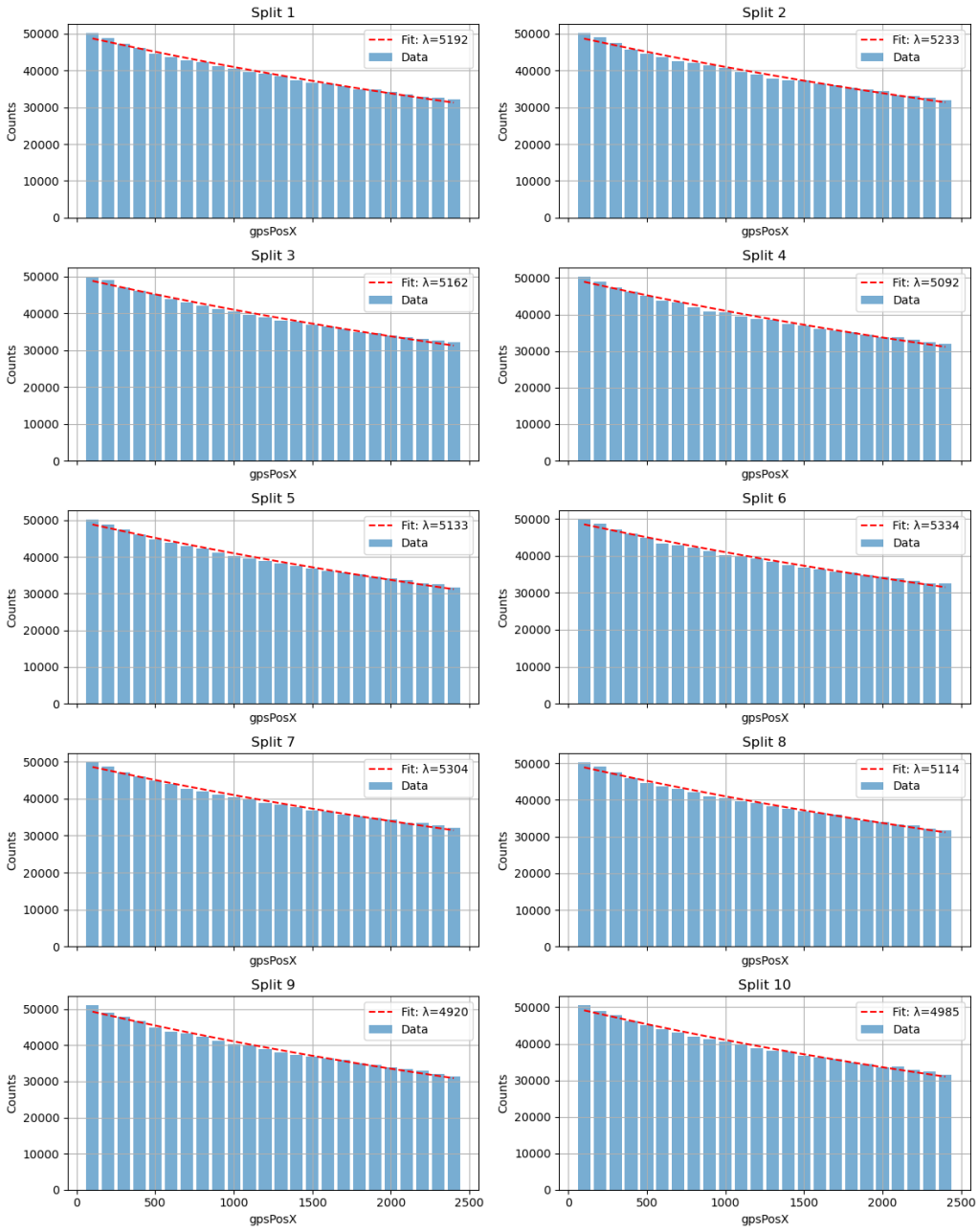

Figure 12: A grid of histograms showing distributions and fits for different ranges of θ.

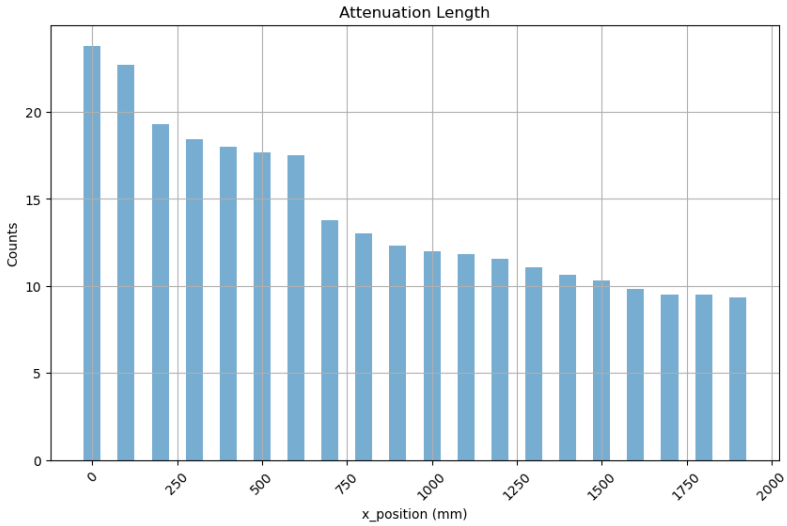

Figure 13: A histogram showing the distribution of the measured intensity over the distance.

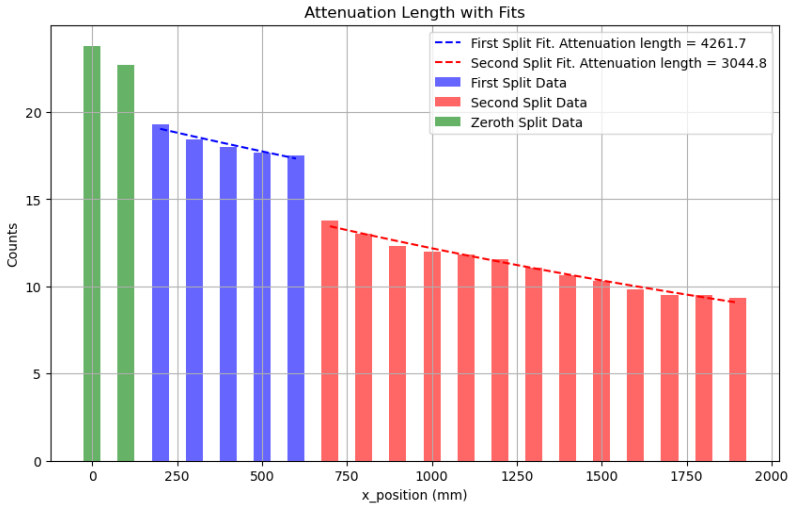

Figure 14: A histogram showing the distribution of the measured intensity, after removing the dark counts, over the distance divided into splits, as well as the fits for the splits.

We notice that this attenuation length is significantly shorter than the one from the simulation data. The most likely explanation here is that in the simulation a different length of attenuation length was considered, than we researched in the lab.

5 Conclusions

In this laboratory experiment we studied a complete characterisation of scintillating fibres used in the LHCb experiment.

We started by exploring the intensity curve by performing spectrometer measurements. In both cases with the light on and off, the results were just as expected and the shape of the intensity with respect to the wavelength was similar. Then we checked the radial symmetry across horizontal and vertical angles in the fibre, which confirms the distribution of the photons as expected.

In the following, we considered simulated data that was provided to us. We performed a data selection to only include physical data, and we calculated the maximum angle theoretically to then compared it with the data we obtained, and found a good alignment between them, ensuring that the simulation is accurate. The angle distributions with respect to the minimal distance of core and clad photons provided a better understanding of the optical phenomena and the propagation of photons through the fibre.

We then compared the attenuation length estimated from both the measurements and the simulated data.
The attenuation length from the simulated data was found to be approximately a length of 5100 mm, and we noticed that there was no clear trend in the attenuation length for different angle bins. Meanwhile the attenuation length of the fibre we researched in the laboratory was found to be approximately 3600 mm, which is shorter than the simulated attenuation length. This difference needs to be checked by further improving the model of the simulation.

In the end, we see a good agreement from the complete analysis of the physical properties of scintillating fibres and the simulation data. All combined gives a full understanding of the scintillating fibres.

References

[1] N H Brook et al. *LHCb RICH 1 Engineering Design Review Report*. en. Aug. 2004. URL: https://cds.cern.ch/record/897981/files/lhcb-2004-121.pdf.

[2] LHCb collaboration et al. "LHCb Detector Performance". en. In: *International Journal of Modern Physics A* 30.07 (Mar. 2015). arXiv:1412.6352 [hep-ex], p. 1530022. ISSN: 0217-751X, 1793-656X. DOI: 10.1142/S0217751X15300227. URL: http://arxiv.org/abs/1412.6352 (visited on 04/16/2024).

[3] Ulisses De Freitas Carneiro Da Graca. "The LHCb SciFi Tracker". In: *PoS* ICHEP2024 (2024), p. 901. DOI: 10.22323/1.476.0901. URL: https://cds.cern.ch/record/2924059.

[4] Lab Course E5a. "Measurement of scintillating fibres for the LHCb experiment." In: (December 2018/June 2023).

[5] Plamen Hopchev. *SciFi: A large Scintillating Fibre Tracker for LHCb*. 2017. arXiv: 1710.08325 [physics.ins-det]. URL: https://arxiv.org/abs/1710.08325.

[6] P. Kopciewicz, S. Maccolini, and T. Szumlak. "The LHCb vertex locator upgrade — the detector calibration overview". en. In: *Journal of Instrumentation* 17.01 (Jan. 2022), p. C01046. ISSN: 1748-0221. DOI: 10.1088/1748-0221/17/01/C01046. URL: https://iopscience.iop.org/article/10.1088/1748-0221/17/01/C01046 (visited on 11/20/2023).

[7] "LHCb - The LHCb Scintillating Fibre Tracker". dimitrios.kaminaris@cern.ch; lukas.witola@cern.ch. 2023. URL: https://cds.cern.ch/record/2883230.

[8] LHCb Collaboration. "LHCb reoptimized detector design and performance : Technical Design Report". In: *CERN-LHCC-2003-030*. Technical Design Report (July 2003). http://cds.cern.ch/record/630827.

[9] "LHCb Tracker Upgrade Technical Design Report". In: (Feb. 2014).

[10] Eduardo Picatoste Olloqui. "LHCb Preshower(PS) and Scintillating Pad Detector (SPD): commissioning, calibration, and monitoring". In: *J. Phys.: Conf. Ser.* 160 (2009), p. 012046. DOI: 10.1088/1742-6596/160/1/012046. URL: https://cds.cern.ch/record/1293075 (visited on 11/20/2023).